

## Post-merger chirps from binary black holes as probes of the final black-hole horizon

Juan Calderon Bustillo <sup>1,2,3,4,5</sup>✉, Christopher Evans <sup>4</sup>✉, James A. Clark<sup>4</sup>, Grace Kim <sup>4,6</sup>, Pablo Laguna<sup>4,7</sup> & Deirdre Shoemaker<sup>4,7</sup>

The merger of a binary black hole gives birth to a highly distorted final black hole. The gravitational radiation emitted as this black hole relaxes presents us with the unique opportunity to probe extreme gravity and its connection with the dynamics of the black hole horizon. Using numerical relativity simulations, we demonstrate a connection between a concrete observable feature in the gravitational waves and geometrical features on the dynamical apparent horizon of the final black hole. Specifically, we show how the line-of-sight passage of a “cusp”-like defect on the horizon of the final black hole correlates with “chirp”-like frequency peaks in the post-merger gravitational-waves. These post-merger chirps should be observed and analyzed as the sensitivity of LIGO and Virgo increase and as future generation detectors, such as LISA and the Einstein Telescope, become operational.

<sup>1</sup>Department of Physics, The Chinese University of Hong Kong, Shatin, N.T., Hong Kong. <sup>2</sup>Monash Centre for Astrophysics, School of Physics and Astronomy, Monash University, Clayton, VIC 3800, Australia. <sup>3</sup>OzGrav: The ARC Centre of Excellence for Gravitational-Wave Discovery, Clayton, VIC 3800, Australia. <sup>4</sup>Center for Relativistic Astrophysics and School of Physics, Georgia Institute of Technology, Atlanta, GA 30332, USA. <sup>5</sup>Instituto Galego de Física de Altas Enerxías, Universidade de Santiago de Compostela, Galicia, Santiago de Compostela, 15782, Spain. <sup>6</sup>Department of Physics and Astronomy, Stony Brook University, Stony Brook, NY 11794, USA. <sup>7</sup>Center for Gravitational Physics, Department of Physics, University of Texas at Austin, Austin, TX 78712, USA. ✉email: [juan.calderon.bustillo@gmail.com](mailto:juan.calderon.bustillo@gmail.com); [cevans216@gatech.edu](mailto:cevans216@gatech.edu)

A new field of astronomy has arisen with the detection of gravitational waves (GWs). To date, the Laser Interferometer Gravitational-wave Observatory (LIGO)<sup>1</sup> and Virgo<sup>2</sup> have observed twelve merging binary black holes (BBHs)<sup>3–7</sup>, two binary neutron star mergers<sup>8,9</sup>, and a putative neutron star-black hole merger<sup>10</sup>. These detections are allowing us to understand the nature of compact objects, their populations<sup>11</sup>, and their formation channels<sup>12,13</sup>. These observations have also put to test general relativity (GR)<sup>14–16</sup> in the strong-field regime for the first time, so far confirming its predictions<sup>17,18</sup>. Despite this groundbreaking achievement, LIGO and Virgo have not yet reached the sensitivity to observe in exquisite detail the merger and the relaxation of the highly distorted black holes (BHs) left behind by BBHs, when dynamical gravity reaches its ultimate expression. As the sensitivity of LIGO and Virgo increases and future generation detectors, such as the Laser Interferometer Space Antenna (LISA) and the Einstein Telescope (ET), become operational, GWs will provide us with an unprecedented view of highly distorted BH horizons, allowing us to test in further detail fundamental aspects of GR like the “no-hair” theorem<sup>15,19</sup> and explore the quantum properties of BHs<sup>20</sup>.

Such studies will rely on a deep understanding of how GW signals encode the dynamical properties of the source. In anticipation of future large signal-to-noise ratio detections, it is important to investigate how GWs reflect not only the “common” properties of BBHs (e.g., BH masses and spins, orbital eccentricity, and orientation) but also other fundamental aspects that can be inferred from the morphology of the signal. For instance, all current observations show a rather simple “chirp” morphology<sup>4</sup>, consisting of a monotonic increase of both frequency and amplitude. Initially, both quantities increase slowly, reflecting the low frequency and tightening of the orbit as the two BHs approach each other<sup>21</sup>. Just before the merger, the two BHs reach speeds comparable to that of light, leading to a rapid rise of both frequency and amplitude<sup>21,22</sup>. Once the BHs merge, a highly distorted BH settles into a Kerr BH radiating exponentially decaying ringdown emission<sup>3,19,23,24</sup>. However, this simple morphology describes the GW signal only when the binary has comparable masses or it is viewed face-on so that the emission is vastly dominated by the so-called quadrupole mode.

In contrast, asymmetric BBHs also show strong GW emission in sub-dominant higher-order modes during the merger and ringdown stages<sup>25</sup>, allowing for GWs with non-trivial morphology complexity<sup>26–28</sup> that may unveil new features of the post-merger dynamics. The connection between the horizon dynamics and the GW emission has been widely studied in two main ways. The first consists of finding correlations between far-field signals and fields near the horizon, revealing close connections between the horizon geometry, the GW flux, and strong-field phenomena such as the anti-kick<sup>29–32</sup>. The second approach has focused on the systematic development of analytical tools that can probe and explain the geometrodynamics of space-time causing such correlations and relate it with the generation of GWs<sup>33–37</sup>. None of these studies discuss a direct link to the GW strain observable by detectors. In this work, we follow the approach of<sup>29–32</sup> to correlate a concrete observable feature of the GW strain to a geometrical property of the final BH horizon.

Using numerical relativity simulations, we show that multiple post-merger frequency peaks (or chirps) can be measured near the orbital plane of unequal-mass binaries. We show that these correlate to the line-of-sight passage of strongly emitting regions of large mean curvature gradient and locally extremal Gaussian curvature, present on the dynamical apparent horizon of the final black hole (BH), which cluster around a “cusp”-like defect on it. Conversely, frequency minima correlate to the passage of the

“smoother” opposite region of the horizon, where curvature gradients are smaller.

## Results and discussion

**Post-merger chirps.** Figure 1a depicts the different stages of a BBH. Figure 1b shows the GW strain time series and time-frequency maps recorded by observers in different locations around a numerically simulated BBH with a mass ratio  $q = m_1/m_2 = 3$ . We perform our numerical simulations using the MAYA code, based on the EINSTEINTOOLKIT<sup>38</sup> (for details, please see the “Methods” section). We use geometrical units in terms of the total mass of the binary  $M = m_1 + m_2$  with the speed of light set to unity. The green vertical line denotes the formation of the common apparent horizon. The “face-on” panel shows the signal observed face-on, showing the “vanilla” chirp structure consistent with current observations<sup>4,5</sup>. The different panels in Fig. 1b show the signals recorded at different positions on the orbital plane.

Some time after the common horizon forms, these signals show a clear drop in the frequency, followed by a secondary peak, or post-merger chirp. Depending on the location of the observer, the chirps occur at different times and involve different peak frequencies and intensities. It is illustrative to compare the signals observed in the direction of the recoil of the final BH<sup>26,28</sup>, (kick-on) to those observed in the opposite direction (kick-off). While the kick-on observer records a secondary chirp with larger amplitude and peak frequency than the first, the converse is measured by the kick-off observer. We find that the secondary chirp is more intense compared to the first one in a direction  $\approx 55^\circ$  away from the final recoil (or kick) direction, measured in the direction of the original orbit. This signal is shown in the rightmost panel, showing a clear “double-chirp”. Notably, we find that this is also true for varying mass ratios. The corresponding signals are shown in Fig. 1c for binaries with mass ratios  $q = 1.1–10$ . These also make evident that the double-chirp signature becomes more pronounced as the binary becomes more asymmetric. We acknowledge that a similar non-trivial post-merger emission, visible in the time-domain, was shown by González et al.<sup>26</sup>, in terms of the Newman–Penrose scalar  $\Psi_4$ . However, its frequency content, which is the departing point of our study and the reason behind the double-chirp name, was not shown.

Analytically, these complex and observer-dependent post-merger waveform morphologies can be explained by the asymmetric interaction of the different quasi-normal emission modes beyond the quadrupole one in different directions around the binary. These modes are triggered during the merger and ringdown of asymmetric binaries and have a larger impact on highly inclined binaries<sup>25,28,39</sup>. However, the clarity of the double-chirp signature suggests a connection to some underlying post-merger feature, similar to how the increase of the frequency during the inspiral is connected to the increasing frequency of the binary. In the following, we argue that this feature is the existence of regions of locally extremal curvature that are distributed non-uniformly on the dynamical apparent horizon of the final BH. While three of these regions cluster around a global curvature maximum that we denote as the “cusp” forming a “trident”, a fourth one sits on the opposite or “back” side of the horizon. These coincide with regions of maximal GW emission. As the final BH relaxes, this structure rotates pointing to all observers on the orbital plane while fading away. We show that after the cusp (back) of the horizon crosses the line-of-sight, frequency peaks (minima) are recorded at a time consistent with the GW travel time determined by the distance to the observer.

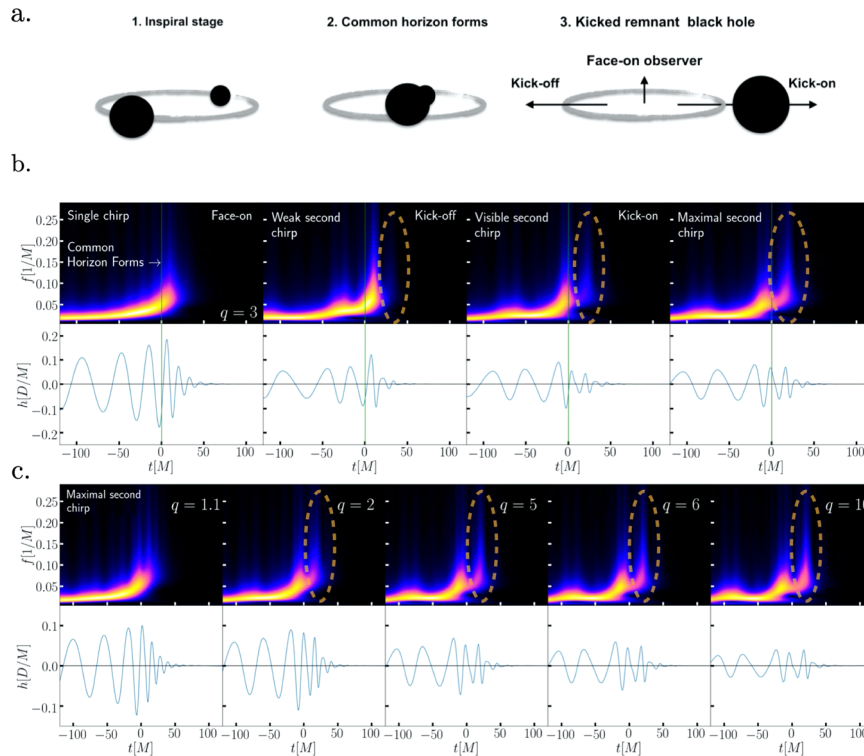


**Fig. 1 Post-merger chirps.** **a** The different stages of a binary black-hole coalescence. **b, c** The strain time series  $h(t)$  of extracted from binary black-hole simulations (white background) and the corresponding time-frequency maps (black background). The green vertical line denotes the instant at which the final common horizon is first found in our simulations. All waveforms include the most dominant modes  $(\ell, m) = \{(2, \pm 1), (2, \pm 2), (3, \pm 2), (3, \pm 3), (4, \pm 3), (4, \pm 4)\}$ . **b** The case of mass ratio  $q = 3$  for different viewing angles (from left to right): face-on, kick-off, kick-on, and  $55^\circ$  away from the kick direction measured in the direction of the orbit, for which the double-chirp feature is most prominent. **c** The signals emitted by binaries with a corresponding mass ratio  $q = 1.1$ -10 in this last direction. The double-chirp feature becomes more pronounced as the mass ratio  $q$  increases.

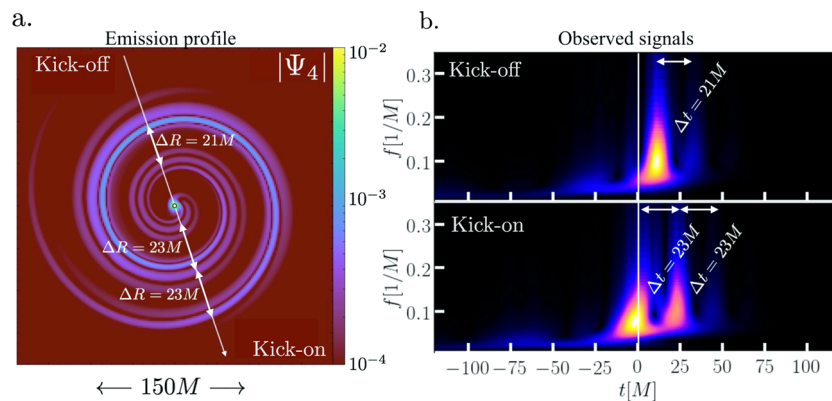


**Fig. 2 Relation between post-merger chirps and arriving gravitational-wave trains.** **a** A snapshot of the gravitational waves in the orbital plane at a time of  $52.3M$  after the merger, for the case of a  $q = 3$  binary. This is expressed in terms of the absolute value of the Newman-Penrose scalar  $\Psi_4$ . We highlight the kick-on and kick-off directions and the separation  $\Delta t \sim \mathcal{O}(20M)$  of the wave trains traveling towards each observer. **b** The corresponding  $\Psi_4$  time-frequency maps recorded by the kick-on and kick-off observers. The time elapsed  $\Delta t \sim \mathcal{O}(20M)$  between frequency peaks (or chirps) is consistent with the separation of the arriving wave trains. Two strong wave trains reach the kick-on observer, which translates into a prominent double-chirp. In contrast, the second front traveling toward the kick-off observer is much weaker, translating into a weak second chirp.

**Emission profile far from the source.** To make a first connection between the time-frequency morphology of the signal and the structure of the GW emission, the left panel of Fig. 2a shows a snapshot of the GW emission in the orbital plane of our  $q = 3$  binary at a time of  $52.3M$  after the merger after the waves have traveled far from the source. We represent the GW emission by the absolute value of the Newman-Penrose scalar  $\Psi_4$ <sup>40</sup>, related to the GW strain  $h$  by  $\Psi_4(t) = \frac{d^2 h^+(t)}{dt^2}$ . As one goes around the final

BH, it is clear that the recorded signal will depend on the viewing angle. This can be, in fact, observed in Fig. 2b, which showcases the time-frequency maps recorded by the kick-on and kick-off observers highlighted in the left panel. The radial separation of  $\Delta R \sim \mathcal{O}(20M)$  between the wave trains reaching each observer in the left panel is consistent with the time delay  $\Delta t \sim \mathcal{O}(20M)$  between frequency peaks shown in the right one. Following the kick-on and kick-off directions, it is also evident that the intensity

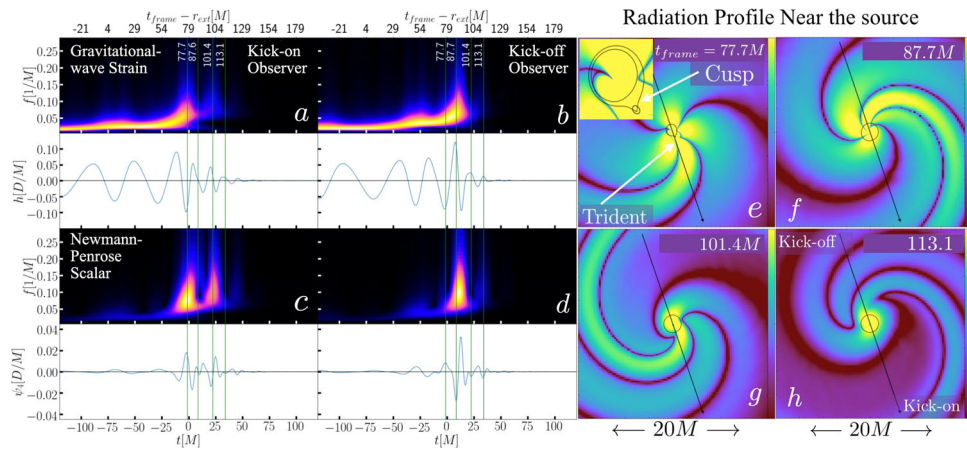


**Fig. 3 Relation between post-merger chirps and the black-hole cusp passage through the line-of-sight.** **a, b** The time-frequency maps and time series of the gravitational-wave strain  $h$ , respectively, observed in the kick-on and kick-off directions, extracted at a distance  $r_{\text{ext}} = 75M$  from the source. **c, d** The same for the Newman-Penrose scalar  $\Psi_4$ . The top time axis shows the retarded time  $t_{\text{frame}} - r_{\text{ext}}$ . The four vertical lines denote retarded times  $t_{\text{frame}} - r_{\text{ext}} = t_{\text{frame},i}$  with the times  $t_{\text{frame},i}$  corresponding to the four simulation snapshots shown in **e-h**. The bottom time axis has been shifted so that  $t = 0$  denotes the time at which the (2, 2) emission mode has its amplitude peak, as it is common in GW data analysis. **e-h** The corresponding four frames of the absolute value of  $\Psi_4$  in the orbital plane of a  $q = 3$  binary, at the times  $t_{\text{frame},i}$  highlighted in **a-d**. Bright yellow regions denote large values of  $|\Psi_4|$  while dark purple regions denote zeros. The black arrow points in the kick-on direction. The inset highlights the initially asymmetric shape of the final black hole. The three-arm (or “trident”) structure of  $\Psi_4$  present on the bottom side of the horizon has its most prominent arm aligned with a “cusp” defect on it.

of the GW fronts is different in each direction. While two wave trains of similar intensity reach the kick-on observer, the second train reaching the kick-off observer has a much lower intensity. Consistently, the kick-on observer records two chirps of similar intensity plus a weak third one, while the second chirp is barely visible for the kick-off observer.

**The near-horizon region.** After making a first connection between the post-merger chirps and the emission profile far from the source, we now zoom in near the source to investigate the connection to the post-merger dynamics. The panels e-h in Fig. 3 show the structure of  $\Psi_4$  near the horizon at four selected times  $t_{\text{frame}}$  throughout its evolution. In the first frame (Fig. 3e), soon after the horizon forms,  $\Psi_4$  shows a clearly asymmetric pattern. Three arms (a central one, most prominent, and two surrounding weaker ones) cluster on one side of the horizon forming a “trident” while another arm is present on the opposite side (or “back”). We note that this structure does not form abruptly at merger but arises smoothly from the pattern it had when the BHs were approaching each other. The inset shows that the central arm sits on a “cusp” defect present on the horizon. The other three frames show how this structure rotates and fades away as the final BH evolves. As this happens, the three arms (in particular the central one) and the back of the BH cross the line of sight of every observer multiple times.

We now draw our attention to the observed signals. The panels a-d in Fig. 3 show the time-frequency maps and time series for the GW strain  $h$  (panels a and b) and  $\Psi_4$  (panels c and d) measured in the kick-on and kick-off directions at retarded times  $t_{\text{frame}} - r_{\text{ext}}$ , with  $r_{\text{ext}}$  denoting the distance to the source, also known as the GW extraction radius. The vertical lines denote the retarded times that correspond to the four frames on Fig. 3b. As the three  $\Psi_4$  arms, and in particular the central, most prominent one, cross the line-of-sight, a frequency peak is measured at a time  $r_{\text{ext}}$  later. This is also noticeable in the time-domain plots in terms of a short instantaneous signal wavelength, consistent with the short separation of the arriving wave-fronts shown in Fig. 2a. Similarly, a frequency minimum is observed  $r_{\text{ext}}$  after the back of the horizon crosses the line of sight. This is reflected in the time-

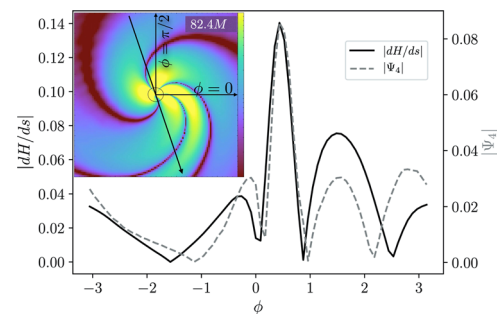


**Fig. 4 Relation between the gravitational-wave emission and mean curvature of the apparent horizon.** The main panel shows the absolute values of the gradient of the mean curvature  $|dH/ds|$  and the Newman-Penrose scalar  $|\Psi_4|$  measured on the intersection of the orbital plane and the final common apparent horizon of a  $q = 3$  binary as a function of the azimuthal angle  $\phi$ , measured  $5M$  after the formation of the common apparent horizon (corresponding to  $t_{\text{frame}} = 82.4$  in e-h of Fig. 3). The parameter  $s$  denotes the arc-length along the equator. The inset shows the corresponding simulation snapshot for  $|\Psi_4|$  measured on the orbital plane.

domain signals by a larger instantaneous wavelength, consistent with the large separation of  $\mathcal{O}(20M)$  of the arriving wave trains shown in Fig. 2a. This way, we establish a time-connection between the line-of-sight passage of the three  $\Psi_4$  arms (in particular the most prominent one) and the back arm and the respective observation of post-merger frequency peaks and minima.

**Connecting the horizon geometry with post-merger chirps.** Next, we connect the arm structure of  $\Psi_4$  present on the dynamical apparent horizon with its curvature. To this, we measure  $\Psi_4$  on the intersection of the horizon with the original orbital plane of the binary (i.e., on the final horizon equator), together with the mean curvature  $H$  and the Gaussian curvature  $K$ . Figure 4 shows the absolute values of the gradient of the mean curvature  $dH/ds$  and  $\Psi_4$  as a function of the azimuthal angle  $\phi$  at a time  $5M$  after the

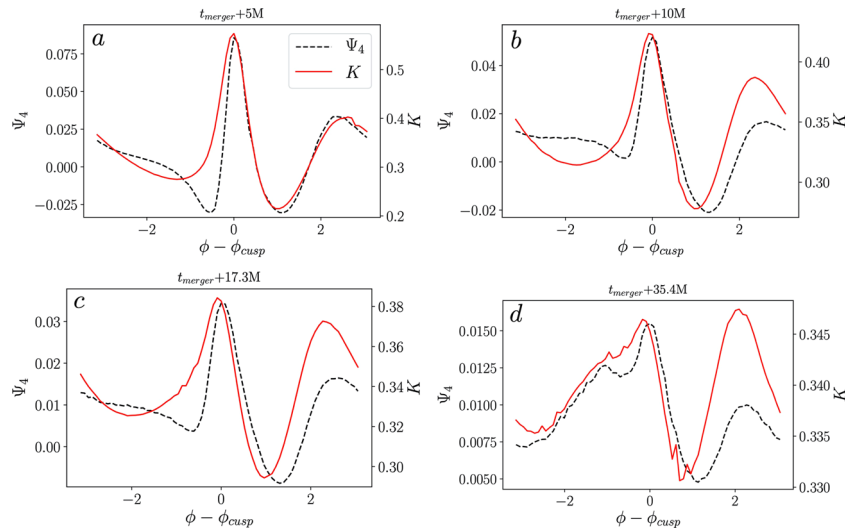


**Fig. 5 Relation between the gravitational-wave emission and Gaussian curvature of the apparent horizon.** Values of the Newman–Penrose scalar  $\Psi_4$  and the Gaussian curvature  $K$  on the intersection of the orbital plane and the final common apparent horizon of a  $q = 3$  binary as a function of the azimuthal angle  $\phi$  at times  $5M$ ,  $10M$ ,  $17.3M$ , and  $35.4M$  after the formation of the common apparent horizon. The x axis has been shifted by a value  $\phi_{\text{cusp}}$  so that the maximum of  $\Psi_4$  (i.e., its central arm) is at  $\phi - \phi_{\text{cusp}} = 0$ .

common horizon has formed. The parameter  $s$  denotes the arc-length along the horizon’s equator (for a detailed description of the arc-length parameter and curvature quantities, please see “Methods” section) and the inset panel shows the corresponding simulation frame. A tight correlation is obvious. In particular, all four  $|\Psi_4|$  maxima, i.e., the arms highlighted in the inset, clearly correspond to local maxima of  $|dH/ds|$ . The three tight  $\Psi_4$  arms correspond to three nearby regions of large  $|dH/ds|$  spanning barely  $\sim 2$  radians, with the maximum of  $|dH/ds|$  (the cusp) matching the maximum of  $|\Psi_4|$ , i.e., the “central” arm.

Figure 5a shows that the  $\Psi_4$  arms also match regions of locally extremal Gaussian curvature  $K$  which, unlike  $H$ , is intrinsic to the apparent horizon and coordinate independent. In Supplementary Fig. 1 and Supplementary Notes I, we show that the same relations hold for all the mass ratios shown in Fig. 1. Moreover, while the location of the apparent horizon itself depends on the gauge choice, we show that these relations also hold in an alternative gauge. Figure 5b–d and those in Supplementary Fig. 2 (and Supplementary Notes II) show that this relation is well preserved throughout the evolution of the final black hole, as the central arm points to the different observers in the orbital plane and the  $\Psi_4$  structure fades away. We observe that a slight degradation of this correlation occurs at very late times of  $\simeq 30M$  after the common horizon has formed when the emission is very weak and more prone to be affected by numerical artefacts. Despite this, the three maxima and minima of  $\Psi_4$  sitting around the central arm are well co-located with those of  $K$ . Also, while here we have used  $|dH/ds|$  to facilitate a visual comparison with the simulation frames, we show that  $\Psi_4$  actually follows  $-dH/ds$ .

Finally, even if not clearly visible Figs. 3e–h and 5 makes also evident that the highly asymmetric structure of the horizon understood as the “clustering” of three  $\Psi_4$  arms and the corresponding extremal curvature regions, is maintained during BH evolution, as these always span an angle that barely exceeds  $\sim 2.5$  radians. This way, the passage of these  $\Psi_4$  arms by the line-of-sight corresponds to the passage of three regions of extremal mean curvature gradient and extremal Gaussian curvature on the horizon, with the central arm corresponding to the cusp.

**Discussion.** The observation of the merger and ringdown stages of BH mergers grants access to the strongest regime of gravity, in

which space-time shows its ultimate phenomenology through the dynamical evolution of highly distorted BH horizons. Connections between these dynamics and the observed BH GWs have been proposed and widely investigated<sup>29–37</sup>. However, no explicit examples of concrete observable features in the GWs have been described to date. In this work, we propose the first such connection. We have shown that non-trivial features consisting on multiple frequency peaks in the post-merger GW emission of edge-on, asymmetric BH mergers, are linked to the presence of large curvature regions in the dynamical apparent horizon of the final BH that is asymmetrically distributed.

First, we have shown that an asymmetric emission pattern forms around the final common horizon, with three arms clustering one side and one on the other. Second, we have shown that frequency peaks, which we refer to as post-merger chirps, are observed in the post-merger signal as the three arms cross the line of sight, after a time consistent with the GW travel time. Last, we show that these arms coincide with locally extremal values of the Gaussian curvature and the mean curvature gradient of the dynamical apparent horizon, with the strongest arm sitting on its largest curvature region, which we call cusp. While post-merger chirps may resemble the signature of BH echoes<sup>20</sup>, these are not, as we are considering standard BHs. For all the mass ratios we have considered, we find this feature is more prominent on the orbital plane of the binary,  $\simeq 55^\circ$  from the final kick direction measured in the direction of the original orbit (or that of the final spin). Nevertheless, we assume that this will be subject to change if spinning BHs were considered<sup>41,42</sup>.

Finally, in the Supplementary Fig. 3 and Supplementary Notes III, we show that Advanced LIGO detectors working at their design sensitivity may observe the post-merger chirp signature for the case of a correctly oriented copy of the BBH GW170729<sup>4,43</sup>, suggesting that such observation may be feasible before the arrival of the next generation of GW detectors.

## Methods

**Time-frequency maps.** The continuous wavelet transform of a function  $g(t)$  is,

$$W(a, b) = \frac{1}{\sqrt{a}} \int_{-\infty}^{\infty} g(t) \psi\left(\frac{t-b}{a}\right) dt, \quad (1)$$

where  $\psi$ , the “mother wavelet”, is a continuous function in time and frequency,

evaluated at scales  $a > 0$  and translations  $b$ . The scale parameter dilates the mother wavelet  $\psi$ , providing a range of time-frequency resolutions, while the translations provide time localization of the signal power,  $|g^2(t)|$ . By selecting for  $\psi$  a function which is compact in the time- and frequency-domains, together with a judicious choice of scales appropriate for the problem at hand, one can use the continuous wavelet transform to resolve substructure in the signal  $g(t)$  of particular physical interest. A complete description of wavelet analysis may be found in ref. 44.

The mother wavelet used in our decomposition is the Morlet wavelet, a Gaussian-modulated sinusoid with minimal compactness in the time- and frequency-domains:  $\psi(x) = \frac{1}{\sqrt{\pi}} \exp(2\pi i f_0 x) - \exp(-2\pi^2 f_0^2) \exp(x^2/2)$ , where  $x = \frac{t-b}{a}$  and  $f_0$  is the frequency of the sinusoid, the center frequency of the wavelet.

As described, the continuous wavelet transform is expressed in terms of mother wavelet dilation scales  $a$ . Our interest lies in the frequency content of the signal, however. It may be shown, by considering the response to a sinusoid of frequency  $f$ , that the maximum of the mother wavelet  $W(a, b)$  lies at  $a = f_0/f$ , so that the focii of the time-frequency response of the signal to the wavelet transform are centered at frequencies  $f = f_0/a$ . For discretized time series data,  $f = F_s f_0/a$ , where  $F_s$  is the sample frequency of the data. We determine empirically, via visual inspection, that a mother wavelet center frequency  $f_0 = 0.4$ , and scales  $a \in [1, 128]$  yield a time-frequency resolution which allows us to resolve the pertinent substructure of the chirping features reported in this work. We have used the pyCWT software library available at <https://pycwt.readthedocs.io/en/latest/> to perform these decompositions numerically.

**Higher modes of the gravitational-wave emission.** The complex GW strain emitted in a direction  $(\iota, \phi)$  on the sky of a BBH can be written as a superposition of different GW modes  $h_{\ell m}(\iota, \phi; t)$  as<sup>45</sup>

$$h(t) = h_+(t) - ih_\times(t) = \sum_{\ell \geq 2} \sum_{m=-\ell}^{m=\ell} Y_{\ell m}^{-2}(\iota, \phi) h_{\ell m}(t). \quad (2)$$

Here,  $h_+$  and  $h_\times$  denote the two GW polarizations, the  $Y_{\ell m}$ 's are spin  $-2$  weighted spherical harmonics, and  $(\iota, \phi)$  are the polar and azimuthal angles of a spherical coordinate system centered on the binary. This is chosen so that,  $\iota = 0$  (face-on) denotes the direction of the orbital angular momentum, while the orbital plane of the binary is located at  $\iota = \pi/2$  (edge-on). For face-on binaries, the quadrupolar  $(\ell, m) = (2, \pm 2)$  modes vastly dominate during all the stages of the binary<sup>45</sup>. As consequence, the frequency of the resulting GW is, to a good approximation, twice the orbital one and the observed signal shows a canonical single chirp morphology. Secondary GW modes are triggered during the merger and ringdown stages and are more visible near the orbital plane of the binary<sup>23,27,28</sup>.

**Computational methodology.** We performed the simulations for this study using our MAYA code<sup>46-49</sup>, a branch of the EINSTEINTOOLKIT<sup>38</sup>. This code was also used to produce the Georgia Tech catalog of gravitational waveforms<sup>50</sup>. We evolve the BSSN formulation of the Einstein equations<sup>51</sup> using the moving puncture gauge condition<sup>52,53</sup> for binary BH systems. The MAYA code is built upon the CACTUS<sup>54</sup> code, using KRANC<sup>55</sup> for code generation and CARPET<sup>56</sup> for mesh refinement. We extract gravitational waveforms from the simulation data using the Newman–Penrose scalar  $\Psi_4$ <sup>57</sup>, which we calculate using the WEYLSCAL4 thorn of the EINSTEINTOOLKIT. We use the AHFINDERDIRECT<sup>58</sup> thorn with minor modifications (see below) to locate and analyze apparent horizons.

**Calculating curvatures on the apparent horizon.** Consider an apparent horizon surface  $\mathcal{S}$  (with 2-metric  $\gamma_{ab}$ ) in a spacelike hypersurface  $\Sigma_t$  (with 3-metric  $g_{ij}$  and associated covariant derivative operator  $\nabla_j$ ). The surface  $\mathcal{S}$  can be defined by the outward-pointing unit normal to the surface  $n^i$ , whose divergence is equal to the mean curvature of the surface  $H = \nabla_i n^i$ .  $H$  is calculated at run time by the AHFINDERDIRECT thorn because it is an extrinsic quantity and therefore more difficult to calculate in post-processing, as it depends on the metric and its derivatives in the neighborhood of horizon. On the other hand, the Gaussian curvature  $K$  of  $\mathcal{S}$  is intrinsic to the surface and can therefore be calculated using only the metric induced on the horizon  $\gamma_{ij} = g_{ij} - n_i n_j$  and its derivatives. We have modified the AHFINDERDIRECT thorn to output  $\gamma_{ij}$  on  $\mathcal{S}$  for this purpose.

On a two-dimensional surface, the Riemann tensor has only one independent component and is therefore completely determined by the Ricci scalar. The Gaussian curvature of  $\mathcal{S}$  is half of the Ricci scalar and is related to components of the Riemann tensor by  $R_{abcd} = K(\gamma_{ac}\gamma_{db} - \gamma_{ad}\gamma_{cb})$ , where the indices  $a, b, c$ , and  $d$  denote the polar  $(\theta)$  and azimuthal  $(\phi)$  angles on the horizon surface. Specifically, we use the  $R_{\theta\phi\theta\phi}$  component of the Riemann tensor in our calculations. Furthermore, by calculating  $K$  in the orbital plane of the binary we significantly reduce the complexity of this expression by taking advantage of the symmetry properties of  $\gamma_{ab}$ .

We compute derivatives with respect to the arc-length parameter  $s$  on the intersection of the orbital plane and the apparent horizon. This is related to the

azimuthal angle  $\phi$  by

$$\frac{ds}{d\phi} = \sqrt{\gamma_{ij} \frac{dx^i dx^j}{d\phi d\phi}} = \sqrt{\gamma_{rr} (\partial_\phi R)^2 + \gamma_{\phi\phi} + 2\gamma_{r\phi} (\partial_\phi R)}. \quad (3)$$

Here,  $R$  denotes the coordinate radius of the horizon. The spherical components of  $\gamma_{ij}$  are related to the cartesian component's output by the AHFINDERDIRECT thorn by:

$$\begin{aligned} \gamma_{rr} &= \cos^2(\phi)\gamma_{xx} + \sin^2(\phi)\gamma_{yy} + \sin(2\phi)\gamma_{xy} \\ \gamma_{\phi\phi} &= r^2 \left[ \sin^2(\phi)\gamma_{xx} + \cos^2(\phi)\gamma_{yy} - \sin(2\phi)\gamma_{xy} \right] \\ \gamma_{r\phi} &= \left[ \frac{1}{2} \sin(2\phi)(\gamma_{xx} - \gamma_{yy}) + \cos(2\phi)\gamma_{xy} \right]. \end{aligned} \quad (4)$$

## Data availability

The numerical relativity waveforms in this work are part of the Georgia Tech catalogue<sup>61</sup> and are publicly available at <http://www.einstein.gatech.edu/table>. The waveforms used are, ordered by mass ratio, are GT0717, GT0446, GT0453, GT0577, GT0604, and GT0568. The curvature and  $\Psi_4$  data for the figures in this work are publicly available at <https://github.com/cevans216/post-merger-chirp-data>.

## Code availability

The numerical evolution code MAYA is available upon request. The PyCBC and pyCWT codes are publicly available.

Received: 5 August 2020; Accepted: 9 September 2020;

Published online: 08 October 2020

## References

- Aasi, J. et al. Advanced LIGO. *Class. Quant. Grav.* **32**, 074001 (2015).
- Acernese, F. et al. Advanced Virgo: a second-generation interferometric gravitational wave detector. *Class. Quant. Grav.* **32**, 024001 (2015).
- Abbott, B. P. et al. Observation of gravitational waves from a binary black hole merger. *Phys. Rev. Lett.* **116**, 061102 (2016).
- Abbott, B. et al. GWTC-1: a gravitational-wave transient catalog of compact binary mergers observed by LIGO and virgo during the first and second observing runs. *Phys. Rev. X* **9**, 031040 (2019).
- The LIGO Scientific Collaboration et al. GW190412: observation of a binary-black-hole coalescence with asymmetric masses. *Phys. Rev. D* **102**, 043015 <https://doi.org/10.1103/PhysRevD.102.043015> (2020).
- Abbott, B. et al. GW190425: observation of a compact binary coalescence with total mass  $\sim 3.4M$ . *Astrophys. J. Lett.* **892**, L3 (2020).
- Abbott et al. GW190521: a binary black hole merger with a total mass of 150  $M$ . *Phys. Rev. Lett.* **125**, 101102 (2020).
- Abbott, B. P. et al. GW170817: observation of gravitational waves from a binary neutron star inspiral. *Phys. Rev. Lett.* **119**, 161101 (2017).
- Abbott, B. P. et al. Gw190425: observation of a compact binary coalescence with total mass  $\sim 3.4M$ . *Astrophys. J.* **892**, L3 (2020).
- Abbott, R. et al. GW190814: Gravitational Waves from the Coalescence of a 23 Solar Mass Black Hole with a 2.6 Solar Mass Compact Object *Astrophys. J. Lett.* **896**, L44 (2020).
- Abbott, B. P. et al. Binary black hole population properties inferred from the first and second observing runs of advanced LIGO and advanced Virgo. *Astrophys. J. Lett.* **882**, L24 (2019).
- Abbott, B. P. et al. Astrophysical implications of the binary black-hole merger GW150914. *Astrophys. J.* **818**, L22 (2016).
- Stevenson, S. P. et al. Formation of the first three gravitational-wave observations through isolated binary evolution. *Nat. Commun.* **8**, 14906 (2017).
- Einstein, A. The foundation of the general theory of relativity. *Ann. Phys.* **49**, 769–822 (1916).
- Misner, C. W., Thorne, K. & Wheeler, J. *Gravitation* (Elsevier, 1974).
- The LIGO Scientific Collaboration et al. Tests of general relativity with the binary black hole signals from the LIGO-Virgo Catalog GWTC-1. *Phys. Rev. D* **100**, 104036 (2019).
- Abbott, B. P. et al. Tests of general relativity with GW150914. *Phys. Rev. Lett.* **116**, 221101 (2016).
- Abbott, B. P. et al. Binary black hole mergers in the first advanced ligo observing run. *Phys. Rev. X* **6**, 041015 (2016).
- Isi, M., Giesler, M., Farr, W. M., Scheel, M. A. & Teukolsky, S. A. Testing the no-hair theorem with GW150914. *Phys. Rev. Lett.* **123**, 111102 (2019).
- Cardoso, V., Hopper, S., Macedo, C. F. B., Palenzuela, C. & Pani, P. Gravitational-wave signatures of exotic compact objects and of quantum corrections at the horizon scale. *Phys. Rev. D* **94**, 084031 (2016).

21. Maggiore, M. *Gravitational Waves. Theory and Experiments* Vol. 1 (Oxford University Press, 2007).
22. Pretorius, F. Evolution of binary black hole spacetimes. *Phys. Rev. Lett.* **95**, 121101 (2005).
23. Berti, E., Cardoso, V. & Starinets, A. O. Quasinormal modes of black holes and black branes. *Class. Quant. Grav.* **26**, 163001 (2009).
24. Owen, R. The final remnant of binary black hole mergers: multipolar analysis. *Phys. Rev. D* **80**, 084012 (2009).
25. Berti, E. et al. Inspiral, merger and ringdown of unequal mass black hole binaries: a multipolar analysis. *Phys. Rev. D* **76**, 064034 (2007).
26. Gonzalez, J. A., Sperhake, U. & Bruegmann, B. Black-hole binary simulations: The Mass ratio 10:1. *Phys. Rev. D* **79**, 124006 (2009).
27. Graff, P. B., Buonanno, A. & Sathyaprakash, B. Missing link: Bayesian detection and measurement of intermediate-mass black-hole binaries. *Phys. Rev. D* **92**, 022002 (2015).
28. Calderón Bustillo, J., Clark, J. A., Laguna, P. & Shoemaker, D. Tracking black hole kicks from gravitational wave observations. *Phys. Rev. Lett.* **121**, 191102 (2018).
29. Rezzolla, L., Macedo, R. P. & Jaramillo, J. L. Understanding the ‘anti-kick’ in the merger of binary black holes. *Phys. Rev. Lett.* **104**, 221101 (2010).
30. Jaramillo, J. L., Panosso Macedo, R., Moesta, P. & Rezzolla, L. Black-hole horizons as probes of black-hole dynamics I: post-merger recoil in head-on collisions. *Phys. Rev. D* **85**, 084030 (2012).
31. Jaramillo, J. L., Macedo, R. P., Moesta, P. & Rezzolla, L. Black-hole horizons as probes of black-hole dynamics II: geometrical insights. *Phys. Rev. D* **85**, 084031 (2012).
32. Jaramillo, J. L., Macedo, R. P., Moesta, P. & Rezzolla, L. Towards a cross-correlation approach to strong-field dynamics in Black Hole spacetimes. *AIP Conf. Proc.* **1458**, 158–173 (2012).
33. Owen, R. et al. Frame-dragging vortexes and tidal tendexes attached to colliding black holes: Visualizing the curvature of spacetime. *Phys. Rev. Lett.* **106**, 151101 (2011).
34. Nichols, D. A. et al. Visualizing spacetime curvature via frame-drag vortexes and tidal tendexes: general theory and weak-gravity applications. *Phys. Rev. D* **84**, 124014 (2011).
35. Zhang, F. et al. Visualizing spacetime curvature via frame-drag vortexes and tidal tendexes. II. stationary black holes. *Phys. Rev. D* **86**, 084049 (2012).
36. Nichols, D. A. et al. Visualizing spacetime curvature via frame-drag vortexes and tidal tendexes. III. quasinormal pulsations of schwarzschild and kerr black holes. *Phys. Rev. D* **86**, 104028 (2012).
37. Prasad, V., Gupta, A., Bose, S., Krishnan, B. & Schnetter, E. News from horizons in binary black hole mergers. *Phys. Rev. Lett.* **125**, 121101 (2020).
38. Löffler, F. et al. The Einstein toolkit: a community computational infrastructure for relativistic astrophysics. *Class. Quant. Grav.* **29**, 115001 (2012).
39. Giesler, M., Isi, M., Scheel, M. A. & Teukolsky, S. A. Black hole ringdown: the importance of overtones. *Phys. Rev. X* **9**, 041060 (2019).
40. Newman, E. & Penrose, R. An approach to gravitational radiation by a method of spin coefficients. *J. Math. Phys.* **3**, 566–578 (1962).
41. Apostolatos, T. A., Cutler, C., Sussman, G. J. & Thorne, K. S. Spin-induced orbital precession and its modulation of the gravitational waveforms from merging binaries. *Phys. Rev. D* **49**, 6274–6297 (1994).
42. Kidder, L. E. Coalescing binary systems of compact objects to (post)5/2-newtonian order. v. spin effects. *Phys. Rev. D* **52**, 821–847 (1995).
43. Chatzioannou, K. et al. On the properties of the massive binary black hole merger GW170729. *Phys. Rev. D* **100**, 104015 (2019).
44. Walnut, D. F. *An Introduction to Wavelet Analysis* (Birkhäuser Boston, 2004).
45. Blanchet, L. Gravitational radiation from post-newtonian sources and inspiralling compact binaries. *Living Rev. Rel.* **17**, 2 (2014).
46. Herrmann, F., Hinder, I., Shoemaker, D. & Laguna, P. Unequal mass binary black hole plunges and gravitational recoil. *Class. Quant. Grav.* **24**, S33–S42 (2007).
47. Vaishnav, B., Hinder, I., Herrmann, F. & Shoemaker, D. Matched filtering of numerical relativity templates of spinning binary black holes. *Phys. Rev. D* **76**, 084020 (2007).
48. Healy, J., Levin, J. & Shoemaker, D. Zoom-Whirl Orbits in Black Hole Binaries. *Phys. Rev. Lett.* **103**, 131101 (2009).
49. Pekowsky, L., O’Shaughnessy, R., Healy, J. & Shoemaker, D. Comparing gravitational waves from nonprecessing and precessing black hole binaries in the corotating frame. *Phys. Rev. D* **88**, 024040 (2013).
50. Jani, K. et al. Georgia tech catalog of gravitational waveforms. *Class. Quant. Grav.* **33**, 204001 (2016).
51. Baumgarte, T. W. & Shapiro, S. L. Numerical integration of Einstein’s field equations. *Phys. Rev. D* **59**, 024007 (1998).
52. Campanelli, M., Lousto, C. O., Marronetti, P. & Zlochower, Y. Accurate evolutions of orbiting black-hole binaries without excision. *Phys. Rev. Lett.* **96**, 111101 (2006).
53. Baker, J. G., Centrella, J., Choi, D.-I., Koppitz, M. & van Meter, J. Gravitational-wave extraction from an inspiraling configuration of merging black holes. *Phys. Rev. Lett.* **96**, 111102 (2006).
54. Goodale, T. et al. The cactus framework and toolkit: design and applications. In *5th International Conference of VECPA Vector and Parallel Processing R’2002* (Springer, Berlin, 2003).
55. Husa, S., Hinder, I. & Lechner, C. Kranc: a mathematica package to generate numerical codes for tensorial evolution equations. *Comput. Phys. Commun.* **174**, 983–1004 (2006).
56. Schnetter, E., Hawley, S. H. & Hawke, I. Evolutions in 3D numerical relativity using fixed mesh refinement. *Class. Quant. Grav.* **21**, 1465 (2004).
57. Reisswig, C., Bishop, N. T., Pollney, D. & Szilágyi, B. Characteristic extraction in numerical relativity: Binary black hole merger waveforms at null infinity. *Class. Quant. Grav.* **27**, 075014 (2010).
58. Thornburg, J. A fast apparent horizon finder for three-dimensional Cartesian grids in numerical relativity. *Class. Quant. Grav.* **21**, 743 (2004).
59. PACE. Partnership for an Advanced Computing Environment (PACE). <http://www.pace.gatech.edu> (2017).
60. Schmidt, P., Harry, I. W. & Pfeiffer, H. P. Numerical relativity injection infrastructure. Preprint at <https://arxiv.org/abs/1703.01076> (2017).
61. Jani, K. et al. Georgia tech catalog of gravitational waveforms. *Class. Quant. Grav.* **33**, 204001 (2016).

## Acknowledgements

We thank Paul D. Lasky and Valentin Christiaens for their comments on the manuscript. Work supported by NSF grants 1505824, 1505524, 1550461, 1908042, 1806580, 1550461, 2003893, XSEDE TG-PHY120016 and NASA 80NSSC19K0322. J.C.B. acknowledges support from the Australian Research Council Discovery Project DP180103155 and the Direct Grant from the CUHK Research Committee with Project ID: 4053406. The project that gave rise to these results also received the support of a fellowship from “la Caixa” Foundation (ID 100010434) and from the European Union’s Horizon 2020 research and innovation programme under the Marie Skłodowska-Curie grant agreement No 847648. The fellowship code is LCF/BQ/PI20/11760016. G.K. acknowledges support from the President’s Undergraduate Research Salary Award of the Georgia Institute of Technology. Computational support through PACE at the Georgia Institute of Technology<sup>59</sup>. The results of Fig. 3 in our Supplementary material made use of the Python Numerical Relativity Injection infrastructure described in ref. <sup>60</sup>. This manuscript has LIGO DCC number P1900139.

## Author contributions

J.C.B. lead the project, noticed the multiple post-merger frequency peaks and its connection to the horizon curvature. C.E. performed the numerical simulations and developed the methods to compute quantities on the apparent horizon. J.C. provided the code to obtain time-frequency maps. G.K. developed the code used to compute sensitive distances. P.L. and D.S. provided key theoretical insights and supervised the work. All authors contributed to the writing and review of the manuscript.

## Competing interests

The authors declare no competing interests.

## Additional information

Supplementary information is available for this paper at <https://doi.org/10.1038/s42005-020-00446-7>.

Correspondence and requests for materials should be addressed to J.C.B. or C.E.

Reprints and permission information is available at <http://www.nature.com/reprints>

Publisher’s note Springer Nature remains neutral with regard to jurisdictional claims in published maps and institutional affiliations.



**Open Access** This article is licensed under a Creative Commons Attribution 4.0 International License, which permits use, sharing, adaptation, distribution and reproduction in any medium or format, as long as you give appropriate credit to the original author(s) and the source, provide a link to the Creative Commons license, and indicate if changes were made. The images or other third party material in this article are included in the article’s Creative Commons license, unless indicated otherwise in a credit line to the material. If material is not included in the article’s Creative Commons license and your intended use is not permitted by statutory regulation or exceeds the permitted use, you will need to obtain permission directly from the copyright holder. To view a copy of this license, visit <http://creativecommons.org/licenses/by/4.0/>.

© The Author(s) 2020